

Implementation of a DNS capability for hypersonic turbulent flows in the high-altitude atmosphere

eCSE07-08

Xiaojun Gu, Charles Moulinec and Jian Fang

Scientific Computing Department,
STFC Daresbury Laboratory, Warrington WA4 4AD



1. Introduction

Non-equilibrium gas flows pose significant modelling challenges and are prevalent in various industrial applications and scientific research areas, such as mass spectrometry, low-pressure environments, vacuum pumps, micro-electro-mechanical systems (MEMS), high-altitude vehicles, and porous media. The Knudsen number (Kn), defined as the ratio of the gas molecular mean free path to the characteristic macroscopic length scale of the flow, quantifies the degree of non-equilibrium.

When the Knudsen number is very small ($Kn < 0.001$), the no-slip boundary condition applies, and continuum theory, specifically the Navier-Stokes-Fourier (NSF) equations, can accurately predict flow fields. In the slip regime ($0.001 < Kn < 0.1$), the NSF equations are applicable if modified to incorporate velocity-slip and temperature-jump at the boundaries. For $Kn > 0.1$, the flow enters the transition regime, where the NSF equations fail to provide accurate predictions. In this regime, kinetic theory approaches, such as the Boltzmann equation or direct simulation Monte Carlo (DSMC), are used. However, the Boltzmann equation's collision term complexity limits its use to simple problems, and DSMC's high computational cost restricts its application to high- Kn flows, 2-D simulations, and low-speed problems that can take weeks to solve. In the early transition regime ($0.1 < Kn < 1$), the moment method is the most effective for capturing rarefied phenomena. It embeds more physical details than the NSF equations while only moderately increasing computational cost.

It has been successfully demonstrated that the moment equations can be applied to a variety of classic problems, including Couette flow, Poiseuille flow, and Kramers' problem, which have all been theoretically studied (Gu et al. 2010; Gu and Emerson 2014). Numerical investigations of 2-D driven cavity flow (Gu et al. 2009) and flow past a circular cylinder (Gu et al. 2019) further showcase the Moment Method potential. However, there is currently no software capable of solving non-equilibrium flows in the early transition regime ($0.1 < Kn < 1$) within 3-D complex geometries with computational efficiency comparable to conventional CFD problems. Understanding flow in the transition regime is crucial for designing, predicting, and operating a wide range of practical devices. Therefore, it is timely and beneficial to develop software that bridges the gap between the continuum approach and kinetic theory.

The project aims to extend the capabilities of the high-order finite-difference method-based computational fluid dynamics (CFD) solver, *ASTR* (Advanced Flow Simulator for Turbulence Research). By developing a new module for the Moment Methods, this extension will enable the research community to investigate and predict shock waves and turbulence in non-equilibrium rarefied gaseous transport up to the early transition regime. These flows present a modelling challenge in hypersonic aerospace engineering applications in high-altitude atmospheres (e.g., 70 km above Earth), involving three fundamental problems: turbulence, shock waves, and rarefaction.

2. Extended thermodynamic governing equations

2.1. Conventional hydrodynamic model - the NSF equations

The traditional hydrodynamic quantities of density, $\bar{\rho}$, velocity, \bar{u}_i , and temperature, \bar{T} , correspond to the first five lowest-order moments of the molecular distribution function. The governing equations of these hydrodynamic quantities for a dilute gas can be obtained from the Boltzmann equation and represent mass, momentum, and energy conservation laws, respectively, in the non-dimensional form consistent with the original implementation in *ASTR*, as:

$$\frac{\partial \rho}{\partial t} + \frac{\partial \rho u_i}{\partial x_i} = 0, \quad (1)$$

$$\frac{\partial \rho u_i}{\partial t} + \frac{\partial \rho u_i u_j}{\partial x_j} + \frac{\partial \sigma_{ij}}{\partial x_j} = - \frac{\partial p}{\partial x_i}, \quad (2)$$

and

$$\frac{\partial E}{\partial t} + \frac{\partial \left((E + p)u_i - \sigma_{ik}u_k + q_i \right)}{\partial x_i} = 0, \quad (3)$$

in which, the non-dimensional variables are defined as

$$u_i = \frac{\bar{u}_i}{u_o}, \quad T = \frac{\bar{T}}{T_o}, \quad \rho = \frac{\bar{\rho}}{\rho_o} \quad \text{and} \quad p = \frac{\bar{p}}{\rho_o u_o^2}, \quad (4)$$

where u_o , T_o and ρ_o are reference velocity, temperature and density, respectively. The spatial and temporal coordinates x_i and t are normalized by a reference geometry length L_o and time scale (L_o/u_o) , respectively, and any suffix i, j, k represents the usual summation convention. The specific heat capacity ratio is γ and the Mach number is defined as

$$Ma = \frac{u_o}{\sqrt{\gamma R T_o}}, \quad (5)$$

with the specific gas constant R . The pressure, p , is related to the temperature and density by the ideal gas law. E in the equation (3) is the non-dimensional volumetric energy, defined as

$$E = \frac{1}{2} \rho u_i^2 + \frac{\rho T}{\gamma(\gamma-1)Ma^2}. \quad (6)$$

However, the stress term, σ_{ij} , and heat flux term, q_i , given in equations (2) and (3) are unknown. The classical way to close this set of equations is through a Chapman-Enskog (CE) expansion of the molecular distribution function around the Maxwellian, in the non-dimensional form, as:

$$\sigma_{ij} = -\frac{2}{A_\sigma \text{Re}} \frac{\partial u_{<i}}{\partial x_{j>}} \quad \text{and} \quad q_i = -\frac{1}{(\gamma-1)Ma^2} \frac{\mu}{A_q \text{Re}} \frac{\partial T}{\partial x_i}, \quad (7)$$

in which μ is the normalised viscosity and the angular brackets denote the traceless part of a symmetric tensor. A_σ and A_q are the collision constants listed in Table 1. The Reynolds number is

$$\text{Re} = \frac{\rho_o u_o L_o}{\mu_o} \quad (8)$$

with a reference viscosity μ_o at the reference temperature T_o . The extent of the non-equilibrium state is determined by the Knudsen number by

$$Kn = \frac{\lambda}{L_o}, \quad (9)$$

in which λ is the mean free path defined as

$$\lambda = \frac{\mu_o}{p_o} \sqrt{\frac{\pi R T_o}{2}}. \quad (10)$$

From equations (5), (8)-(10), it is ready to get the relationship of Kn , Ma and Re as

$$Kn = \sqrt{\frac{\gamma\pi}{2}} \frac{Ma}{\text{Re}}. \quad (11)$$

It indicates that either the increase of the Mach number or the decrease of the Reynolds number can lead to the gas away from the equilibrium state.

2.2. A second-moment closure model - the R13 equations

As the value of Kn increases, more moments are needed to accurately describe any non-equilibrium phenomena. Grad (1949) truncated the distribution function to the incomplete third-order in Hermite polynomials (f_{G13}). Grad was one of the pioneers to introduce σ_{ij} and q_i as extended variables and derived a set of governing equations for them from the Boltzmann equation. For Maxwell molecules, the stress and heat flux equations are (Struchtrup 2005), in the non-dimensional form, as:

$$\frac{\partial \sigma_{ij}}{\partial t} + \frac{\partial u_k \sigma_{ij}}{\partial \bar{x}_k} + \frac{\partial m_{ijk}}{\partial x_k} = -\text{Re} \frac{p}{\mu} \sigma_{ij} - 2p \frac{\partial u_{<i}}{\partial x_{j>}} - \frac{4}{5} \frac{\partial q_{<i}}{\partial x_{j>}} - 2\sigma_{k<i} \frac{\partial u_{j>}}{\partial x_k}, \quad (12)$$

and

$$\begin{aligned} \frac{\partial q_i}{\partial t} + \frac{\partial u_j q_i}{\partial x_j} + \frac{1}{2} \frac{\partial R_{ij}}{\partial x_j} = & -A_q \text{Re} \frac{p}{\mu} q_i - \frac{p}{(\gamma-1)Ma^2} \frac{\partial T}{\partial x_i} - \frac{7\sigma_{ik}}{2\gamma Ma^2} \frac{\partial T}{\partial \bar{x}_k} - \frac{T}{\gamma Ma^2} \frac{\partial \sigma_{ik}}{\partial x_k} \\ & + \frac{\sigma_{ij}}{\rho} \left(\frac{\partial p}{\partial x_j} + \frac{\partial \sigma_{jk}}{\partial x_k} \right) - \frac{2}{5} \left(\frac{7}{2} q_k \frac{\partial u_i}{\partial x_k} + q_k \frac{\partial u_k}{\partial x_i} + q_i \frac{\partial u_k}{\partial x_k} \right) - \frac{1}{6} \frac{\partial \Delta}{\partial x_i} - m_{ijk} \frac{\partial u_j}{\partial \bar{x}_k}. \end{aligned} \quad (13)$$

Here, m_{ijk} , R_{ij} and Δ represent the difference between the true value of the higher moments and their approximated value with f_{G13} . In Grad's original approach, such deviations were not introduced, so that $m_{ijk} = R_{ij} = \Delta = 0$ which results in the well-known G13 equations. To close the set of equations, (1)-(3), (12) and (13), Struchtrup & Torrilhon (2003) and Struchtrup (2005) regularised the G13 equations and obtained the following closures, in the non-dimensional form, as:

$$m_{ijk} = -\frac{\mu}{\text{Re} A_m p} \left[\frac{3T}{\gamma Ma^2} \frac{\partial \sigma_{<ij}}{\partial x_{k>}} + \frac{3\sigma_{<ij}}{\gamma Ma^2} \frac{\partial T}{\partial x_{k>}} - 3 \frac{\sigma_{<ij}}{\rho} \left(\frac{\partial p}{\partial x_{k>}} + \frac{\partial \sigma_{k>l}}{\partial x_l} \right) + \frac{12}{5} q_{<i} \frac{\partial u_j}{\partial \bar{x}_{k>}} \right] \quad (14)$$

$$\begin{aligned} R_{ij} = & -\frac{28}{5A_{R1}} \frac{\mu}{\text{Re} p} \left[\frac{T}{\gamma Ma^2} \frac{\partial q_{<i}}{\partial x_{j>}} + \frac{2}{\gamma Ma^2} q_{<i} \frac{\partial T}{\partial x_{j>}} + \frac{5T}{7\gamma Ma^2} \left(\sigma_{k<i} \frac{\partial u_{j>}}{\partial x_k} + \sigma_{k<i} \frac{\partial u_k}{\partial x_{j>}} - \frac{2}{3} \sigma_{ij} \frac{\partial u_k}{\partial x_k} \right) \right. \\ & \left. - \frac{q_{<i}}{\rho} \left(\frac{\partial p}{\partial x_{j>}} + \frac{\partial \sigma_{j>k}}{\partial \bar{x}_k} \right) - \frac{5}{6} \frac{\sigma_{ij}}{\rho} \left(\frac{\partial q_k}{\partial x_k} + \sigma_{kl} \frac{\partial u_k}{\partial x_l} \right) \right] - \frac{A_{R2}}{A_{R1}} \frac{\sigma_{k<i} \sigma_{j>k}}{\rho}, \end{aligned} \quad (15)$$

and

$$\Delta = -\frac{8}{A_{\Delta 1}} \frac{\mu}{\text{Re} p} \left[\frac{7}{2} \frac{q_k}{\gamma Ma^2} \frac{\partial T}{\partial \bar{x}_k} + \frac{T}{\gamma Ma^2} \left(\frac{\partial q_k}{\partial x_k} + \sigma_{ij} \frac{\partial u_i}{\partial x_j} \right) - \frac{q_j}{\rho} \left(\frac{\partial p}{\partial x_j} + \frac{\partial \sigma_{jk}}{\partial x_k} \right) \right] - \frac{A_{\Delta 2}}{A_{\Delta 1}} \frac{\sigma_{ij} \sigma_{ij}}{\bar{\rho}}. \quad (16)$$

Struchtrup (2005) denoted this set of 13-moment equations with the above closure as the R13 equations.

2.3. Extending the hydrodynamic model - the R26 equations

It was found (Gu *et al.* 2010; Young 2011; Gu & Emerson 2014) that the R13 equation set is not adequate enough to capture the Knudsen layer in Kramers' problem and the regularised 26-moment equations (R26) are required to accurately reproduce the velocity defect found with kinetic data. However, both the R13 and R26 equations are able to capture many of the non-equilibrium phenomena observed using kinetic theory. These include effects such as the tangential heat flux in planar Couette flow and the bimodal temperature profile in planar force-driven Poiseuille flow (Taheri & Struchtrup 2009; Taheri *et al.* 2009; Gu & Emerson 2007, 2009). Since equations (14) and (15) are algebraic approximations for m_{ijk} and R_{ij} , they have no mechanism to produce a boundary layer for themselves near the wall. Alternatively, the governing equations of m_{ijk} , R_{ij} and Δ derived from the Boltzmann equation can be used to provide information required in equations (12) and (13). They are (Gu & Emerson 2009):

$$\begin{aligned} \frac{\partial m_{ijk}}{\partial t} + \frac{\partial u_l m_{ijk}}{\partial x_l} + \frac{\partial \phi_{ijkl}}{\partial x_l} = & -\text{Re} A_m \frac{p}{\mu} m_{ijk} - \frac{3}{\gamma Ma^2} \frac{\partial T \sigma_{<ij}}{\partial x_{k>}} - \frac{3}{7} \frac{\partial R_{<ij}}{\partial x_{k>}} + 3 \frac{\sigma_{<ij}}{\rho} \left(\frac{\partial \sigma_{k>l}}{\partial x_l} + \frac{\partial p}{\partial x_{k>}} \right) \\ & - \frac{12}{5} q_{<i} \frac{\partial u_j}{\partial x_{k>}} - 3m_{l<ij} \frac{\partial u_{k>}}{\partial x_l} \end{aligned} \quad (17)$$

$$\begin{aligned}
\frac{\partial R_{ij}}{\partial t} + \frac{\partial u_k R_{ij}}{\partial x_k} + \frac{\partial \psi_{ijk}}{\partial x_k} = & -A_{R1} \text{Re} \frac{p}{\mu} R_{ij} - \frac{28}{5} \frac{T}{\gamma Ma^2} \frac{\partial q_{<i}}{\partial x_{j>}} + \left(\frac{8}{3} \frac{T \sigma_{ij}}{\gamma Ma^2} - \frac{2}{7} R_{ij} \right) \frac{\partial u_k}{\partial x_k} \\
& - \frac{4}{7} \left(\frac{7}{\gamma Ma^2} T \sigma_{k<i} + R_{k<i} \right) \left(\frac{\partial u_{j>}}{\partial x_k} + \frac{\partial u_k}{\partial x_{j>}} \right) - 2R_{k<i} \frac{\partial u_{j>}}{\partial x_k} + \frac{28}{5} \frac{q_{<i}}{\rho} \frac{\partial \sigma_{j>k}}{\partial x_k} \\
& + \frac{28}{5} \frac{T}{\gamma Ma^2} q_{<i} \left(\frac{\partial p}{p \partial x_{j>}} - 2 \frac{\partial T}{T \partial x_{j>}} \right) - \frac{14}{15} \Delta \frac{\partial u_{<i}}{\partial x_{j>}} + 2 \frac{m_{ijk}}{\rho} \frac{\partial \sigma_{kl}}{\partial x_l} \\
& + m_{ijk} \left(\frac{2}{\rho} \frac{\partial p}{\partial x_k} - \frac{9}{\gamma Ma_2} \frac{\partial T}{\partial x_k} \right) + \frac{14}{3} \frac{\sigma_{ij}}{\rho} \left(\frac{\partial q_m}{\partial x_m} + \sigma_{ml} \frac{\partial u_m}{\partial x_l} \right) \\
& - \frac{2T}{\gamma Ma^2} \frac{\partial m_{ijk}}{\partial x_k} - \frac{2}{5} \frac{\partial \Omega_{<i}}{\partial x_{j>}} - 2\phi_{ijkl} \frac{\partial u_k}{\partial x_l} - A_{R2} \text{Re} \frac{p}{\mu} \frac{\sigma_{k<i} \sigma_{j>k}}{\rho}
\end{aligned} \tag{18}$$

and

$$\begin{aligned}
\frac{\partial \Delta}{\partial t} + \frac{\partial \Delta u_i}{\partial x_i} + \frac{\partial \Omega_i}{\partial x_i} = & -A_{\Delta 1} \text{Re} \frac{p}{\mu} \Delta - \frac{8T}{\gamma Ma^2} \frac{\partial q_k}{\partial x_k} - \frac{4}{3} \Delta \frac{\partial u_k}{\partial x_k} + \frac{T q_k}{\gamma Ma_2} \left(8 \frac{\partial p}{p \partial x_k} - 28 \frac{\partial T}{T \partial x_k} \right) \\
& - 4 \left(2 \frac{T \sigma_{kl}}{\gamma Ma^2} + R_{kl} \right) \frac{\partial u_k}{\partial x_l} + 8 \frac{q_k}{\rho} \frac{\partial \sigma_{kl}}{\partial x_l} - A_{\Delta 2} \text{Re} \frac{p}{\mu} \frac{\sigma_{kj} \sigma_{jk}}{\rho}
\end{aligned} \tag{19}$$

Here, ϕ_{ijkl} , ψ_{ijk} and Ω_i are the difference between the true value of the higher moments and their approximated value with f_{G26} . In the R26 equations (Gu & Emerson 2009), they were obtained by a Chapman-Enskog expansion. For convenience, they can be expressed as gradient transport terms and high-order nonlinear terms, respectively, by

$$\left\{ \begin{aligned} \phi_{ijkl} &= -\frac{\mu}{A_{\phi 1} \text{Re} \rho} \left(4 \frac{\partial m_{<ijk}}{\partial x_{l>}} \right) + \phi_{ijkl}^{NL}, \\ \psi_{ijk} &= -\frac{27\mu}{7 \text{Re} A_{\psi 1} \rho} \frac{\partial R_{<ij}}{\partial x_{k>}} + \psi_{ijk}^{NL}, \\ \Omega_i &= -\frac{\mu}{A_{\Omega 1} \text{Re} \rho} \left(\frac{7}{3} \frac{\partial \Delta}{\partial x_i} + 4 \frac{\partial R_{ik}}{\partial x_k} \right) + \Omega_i^{NL}, \end{aligned} \right. \tag{20}$$

Here ϕ_{ijkl}^{NL} , ψ_{ijk}^{NL} and Ω_i^{NL} are the remaining nonlinear high-order terms of ϕ_{ijkl} , ψ_{ijk} and Ω_i , respectively and are provided by Gu and Emerson (2009). They are not implemented in the current version of the code. The values of the collision constants, A_σ , A_q , A_m , A_{R1} , A_{R2} , $A_{\Delta 1}$, $A_{\Delta 2}$, A_ϕ , A_ψ and A_Ω , depend on the molecular collision model adopted and represent the relaxation time scale for each moment. They are given in Table 1 for the case of Maxwell molecules (Truesdell & Muncaster 1980; Struchtrup 2005), as employed in the present study. Although a dilute monatomic gas is employed, all the findings in the present study have relevance to realistic gases, such as air.

A_σ	A_q	A_m	A_{R1}	A_{R2}	$A_{\Delta 1}$	$A_{\Delta 2}$	A_ϕ	A_ψ	A_Ω
1.0	2/3	3/2	7/6	2/3	2/3	2/3	2.097	1.698	1.0

TABLE 1. Collision constants in the moment equations for Maxwell molecules

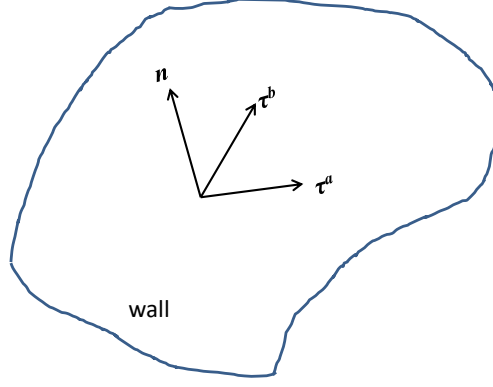


Figure 1: Orientation of a solid wall

3. Wall boundary conditions

To apply any of the foregoing models to flows in confined geometries, appropriate wall boundary conditions are required to determine a unique solution. Gu & Emerson (2009) obtained a set of wall boundary conditions for the R26 equations based on Maxwell's kinetic wall boundary condition (Maxwell 1879) and a fifth-order approximation of the molecular distribution function in Hermite polynomials. In a frame where the coordinates are attached to the wall as shown in figure 1, with n_i the normal vector out of the wall pointing towards the gas and τ_i the tangential vector of the wall, the slip velocity parallel to the wall, u_τ , and temperature-jump conditions are:

$$u_\tau = \left[-\frac{2-\alpha}{\alpha} \sqrt{\frac{\pi}{2}} \sqrt{\frac{T}{\gamma Ma^2}} \sigma_{n\tau} - \frac{q_\tau}{5} - \frac{m_{m\tau}}{2} + \frac{\gamma Ma^2}{T} \frac{9\Omega_\tau + 70\psi_{m\tau}}{2520} \right] \frac{1}{p_\alpha} \quad (21)$$

and

$$(T - T_w) = \left[-\frac{2-\alpha}{\alpha} \sqrt{\frac{\pi}{2}} \sqrt{\frac{T}{\gamma Ma^2}} \frac{q_n}{2} - \frac{T}{\gamma Ma^2} \frac{\sigma_{nn}}{4} + p_\alpha \frac{u_\tau^2}{4} - \frac{75R_{nn} + 28\Delta}{840} + \frac{\phi_{nnnn}}{24} \right] \frac{\gamma Ma^2}{p_\alpha} \quad (22)$$

where

$$p_\alpha = p + \frac{\sigma_{nn}}{2} - \frac{\gamma Ma^2}{T} \left(\frac{30R_{nn} + 7\Delta}{840} + \frac{\phi_{nnnn}}{24} \right) \quad (23)$$

Here σ_m , $\sigma_{n\tau}$, q_τ , $m_{m\tau}$, m_{nnn} , R_{nn} , $\psi_{m\tau}$, Ω_τ and ϕ_{nnnn} are the tangential and normal components of σ_{ij} , q_i , m_{ijk} , R_{ij} , ψ_{ijk} , Ω_i and ϕ_{ijkl} relative to the wall, respectively. It should be noted that the normal velocity at the wall, $u_n = 0$, since there is no gas flow through the wall. The accommodation coefficient, α , represents the fraction of gas molecules which will be *diffusively* reflected with a Maxwellian distribution at the temperature of the wall, T_w . The remaining fraction $(1-\alpha)$ of gas molecules will undergo *specular* reflection. Equations (21) and (22) are similar to the velocity-slip and temperature-jump conditions for the NSF equations (Cercignani 1975; Gad-el-Hak 1999) with the additional underlined terms on the right hand side providing the higher-order moment contributions which are not available in the NSF model. However, these higher-order moment terms can be used to derive a second-order slip boundary condition for the NSF equations (Taheri & Struchtrup 2010). The solution of the NSF equations in the present study is associated with the wall boundary conditions (21) and (22) without the underlined terms. The rest of the wall boundary conditions in non-dimensional form are:

$$\sigma_{\tau\tau} = \left\{ -\frac{2-\alpha}{\alpha} \sqrt{\frac{\pi}{2}} \sqrt{\frac{T}{\gamma Ma^2}} \left(\frac{5m_{n\tau\tau} + 2q_n}{5} \right) - \frac{R_{\tau\tau} + R_{nn}}{14} - \frac{\Delta}{30} - \frac{\phi_{m\tau\tau}}{2} \right\} \frac{\gamma Ma^2}{T} + p_\alpha (\hat{u}_\tau^2 + \hat{T}_w - 1), \quad (24)$$

$$\sigma_{mn} = \left\{ -\frac{2-\alpha}{\alpha} \sqrt{\frac{\pi}{2}} \sqrt{\frac{T}{\gamma Ma^2}} \left(\frac{5m_{nmn} + 6q_n}{10} \right) - \left(\frac{R_{mn}}{7} + \frac{\Delta}{30} + \frac{\phi_{nmn}}{6} \right) \right\} \frac{\gamma Ma^2}{T} + p_\alpha (\hat{T}_w - 1), \quad (25)$$

$$q_\tau = -\frac{5}{18} \frac{2-\alpha}{\alpha} \sqrt{\frac{\pi}{2}} \sqrt{\frac{T}{\gamma Ma^2}} \left(7\sigma_{n\tau} + \frac{\gamma Ma^2}{T} R_{n\tau} \right) - \frac{10m_{m\tau}}{9} - \left(\frac{5\psi_{m\tau}}{81} + \frac{\Omega_\tau}{56} \right) \frac{\gamma Ma^2}{T} - \frac{5\hat{u}_\tau p_\alpha (\hat{u}_\tau^2 + 6\hat{T}_w)}{18} \sqrt{\frac{T}{\gamma Ma^2}}, \quad (26)$$

$$m_{\tau\tau\tau} = -\frac{2-\alpha}{\alpha} \sqrt{\frac{\pi}{2}} \sqrt{\frac{T}{\gamma Ma^2}} \left(3\sigma_{n\tau} + \frac{\gamma Ma^2}{T} \left(\frac{3}{7} R_{n\tau} + \phi_{n\tau\tau\tau} \right) \right) - p_\alpha \hat{u}_\tau \sqrt{\frac{T}{\gamma Ma^2}} (\hat{u}_\tau^2 + 3\hat{T}_w) - \frac{3m_{m\tau}}{2} - \frac{9q_\tau}{5} - \left(\frac{9\Omega_\tau}{280} + \frac{2\psi_{\tau\tau\tau} + 3\psi_{m\tau}}{36} \right) \frac{\gamma Ma^2}{T}, \quad (27)$$

$$m_{m\tau} = -\frac{2-\alpha}{\alpha} \sqrt{\frac{\pi}{2}} \sqrt{\frac{T}{\gamma Ma^2}} \left(\sigma_{\tau n} + \frac{\gamma Ma^2}{T} \left(\frac{R_{n\tau}}{7} + \frac{\phi_{nm\tau}}{3} \right) \right) - \frac{2}{5} q_\tau - \left(\frac{\psi_{m\tau}}{18} + \frac{\Omega_\tau}{140} \right) \frac{\gamma Ma^2}{T} - \frac{2\hat{T}_w \hat{u}_\tau p_\alpha}{3} \sqrt{\frac{T}{\gamma Ma^2}}, \quad (28)$$

$$R_{\tau\tau} = -\frac{2-\alpha}{\alpha} \sqrt{\frac{\pi}{2}} \sqrt{\frac{T}{\gamma Ma^2}} \left(\frac{28q_n}{15} + \frac{14m_{n\tau\tau}}{3} + \frac{\gamma Ma^2}{T} \left(\frac{\Omega_n}{15} + \frac{14\psi_{n\tau\tau}}{27} \right) \right) - \frac{R_{mn}}{3} - \frac{14\Delta}{45} - \frac{7(\phi_{\tau\tau\tau} + 3\phi_{m\tau\tau})}{9} + \left(\frac{7p_\alpha (\hat{u}_\tau^4 + 6\hat{T}_w \hat{u}_\tau^2 + 3\hat{T}_w^2 - 3)}{9} - \frac{14\sigma_{\tau\tau}}{3} \right) \frac{T}{\gamma Ma^2}, \quad (29)$$

$$R_{mn} = -\frac{2-\alpha}{\alpha} \sqrt{\frac{\pi}{2}} \sqrt{\frac{T}{\gamma Ma^2}} \left(\frac{21q_n}{8} + \frac{35m_{nmn}}{16} + \frac{\gamma Ma^2}{T} \left(\frac{35\psi_{nmn}}{144} + \frac{3\Omega_n}{32} \right) \right) - \frac{7\Delta}{30} - \frac{7\phi_{nmn}}{6} + \frac{T}{\gamma Ma^2} \left(\frac{7p_\alpha (\hat{T}_w^2 - 1)}{4} - \frac{7\sigma_{mn}}{2} \right), \quad (30)$$

$$\Delta = -\frac{35}{4} \frac{2-\alpha}{\alpha} \sqrt{\frac{\pi}{2}} \sqrt{\frac{T}{\gamma Ma^2}} \left(q_n + \frac{\gamma Ma^2}{T} \frac{\Omega_n}{28} \right) - \frac{15}{8} R_{mn} + \frac{35}{48} \phi_{nmn} - \frac{5}{4} \frac{T}{\gamma Ma^2} \left(p_\alpha \left(6 - 6\hat{T}_w^2 - \frac{\hat{u}_\tau^4}{4} - 3\hat{u}_\tau^2 \hat{T}_w \right) + 3\sigma_{mn} \right), \quad (31)$$

in which, $\hat{u}_\tau = u_\tau / \sqrt{RT}$ and $\hat{T}_w = T_w / T$.

4. Validations

Different types of geometry were used to test the implementation. The three-dimensional Talor-Green Vortex (TGV) test case is used to test the implementation of the equations and the case of the two-dimensional lid-driven cavity flow is used to test the implementation of the equations and the wall boundary condition.

4.1 Taylor-Green Vortex test case

The Taylor-Green Vortex (TGV) is a well-known benchmark problem in fluid dynamics, often used to test the accuracy and robustness of numerical methods for turbulence, compressible flows, and rarefied gas dynamics. It represents a decaying vortex system, where the initial large-scale vortical structures break down into smaller scales due to nonlinear interactions, eventually leading to turbulence or dissipation. Its significance lies in its ability to assess the accuracy of different numerical schemes and physical models, particularly in capturing vortex dynamics, energy dissipation, and the transition to turbulence. For high-Mach and low-Reynolds-number cases, the TGV serves as a valuable test case for hypersonic and rarefied flow regimes, providing a means to validate moment models, kinetic methods, and continuum breakdown predictions by comparing results with Direct Simulation Monte Carlo (DSMC) or other reference solutions.

The initial velocity distribution for the three-dimensional TGV is given as,

$$\begin{cases} u = u_o \sin(x/L_o) \cos(y/L_o) \cos(z/L_o) \\ v = -u_o \cos(x/L_o) \sin(y/L_o) \cos(z/L_o) \\ w = 0 \end{cases} \quad (32)$$

with the initial pressure field:

$$p = p_o + \frac{\rho_o u_o^2}{160\gamma} [\cos(2x/L_o) + \cos(2y/L_o)] [\cos(2z/L_o) + 2], \quad (33)$$

which are shown in figure 2.

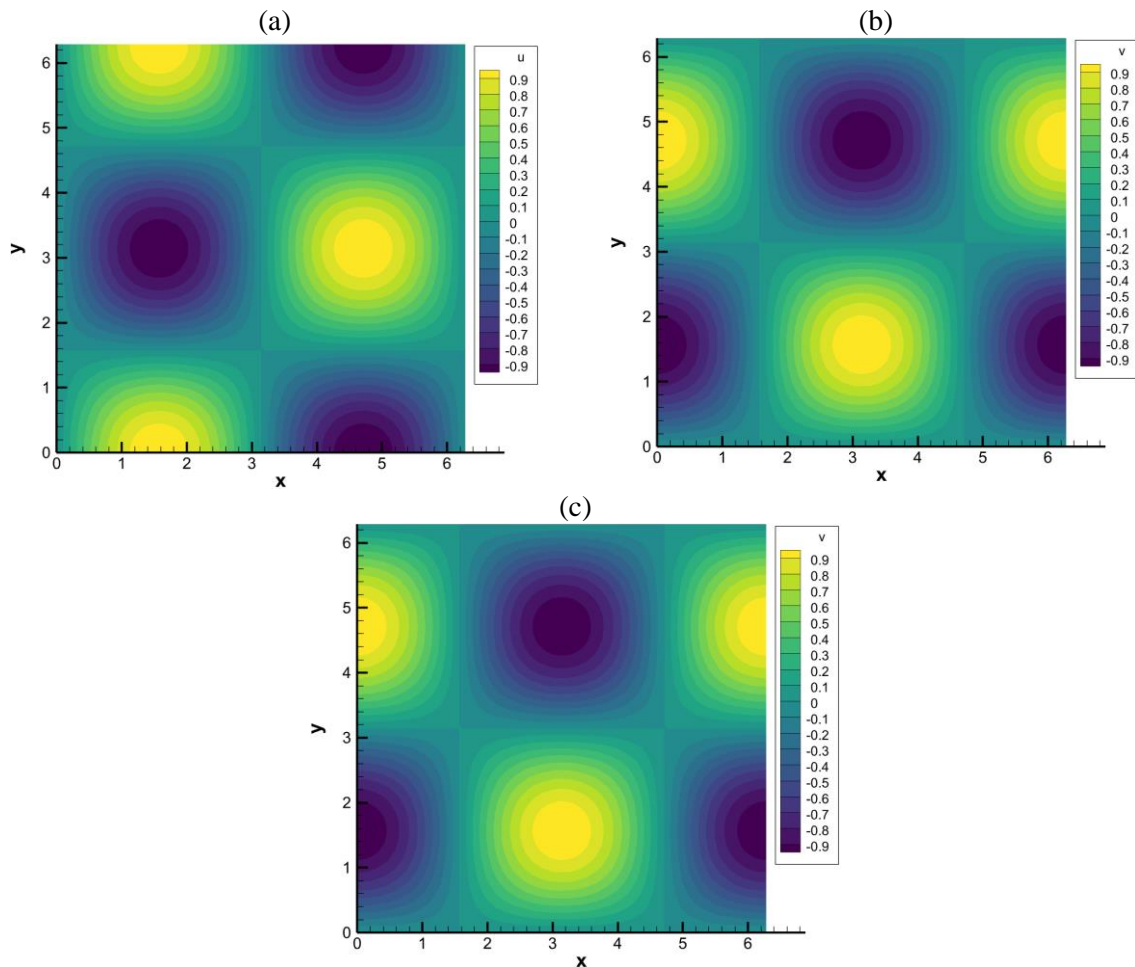


Figure 2 Initial velocity and pressure field of the TGV flow.

We first validate the development of the R13 model at a low Knudsen number ($Kn=0.01$), from which we expect a consistent result between NSF and R13. The TGV was solved within a 3-D box computational domain with size $2\pi^3$ and the domain was meshed with 128^3 and 256^3 grid points, respectively. The reference Reynolds number and Mach number are respectively $Re=450$ and $Ma=0.3$, leading to a Knudsen number $Kn=0.001$, which is a weak rarefied flow. The evolution of the kinetic energy and dissipation rate are compared with the data obtained with Nek5000 and DSMC (Gallis *et al.* 2017) in figure 3(a). The evolution of kinetic energy from different methods collapsed, meaning the statistics are not sensitive to the closure of high-order moments. But with a detailed comparison of the dissipation rate in figure 3 (b), we note the result from the R13 agrees better with the result from DSMC slightly. By calculating the difference in dissipation rate in figure 3 (c), we can see the difference between the NSF and R13 model is between 0.6%, which is negligible.

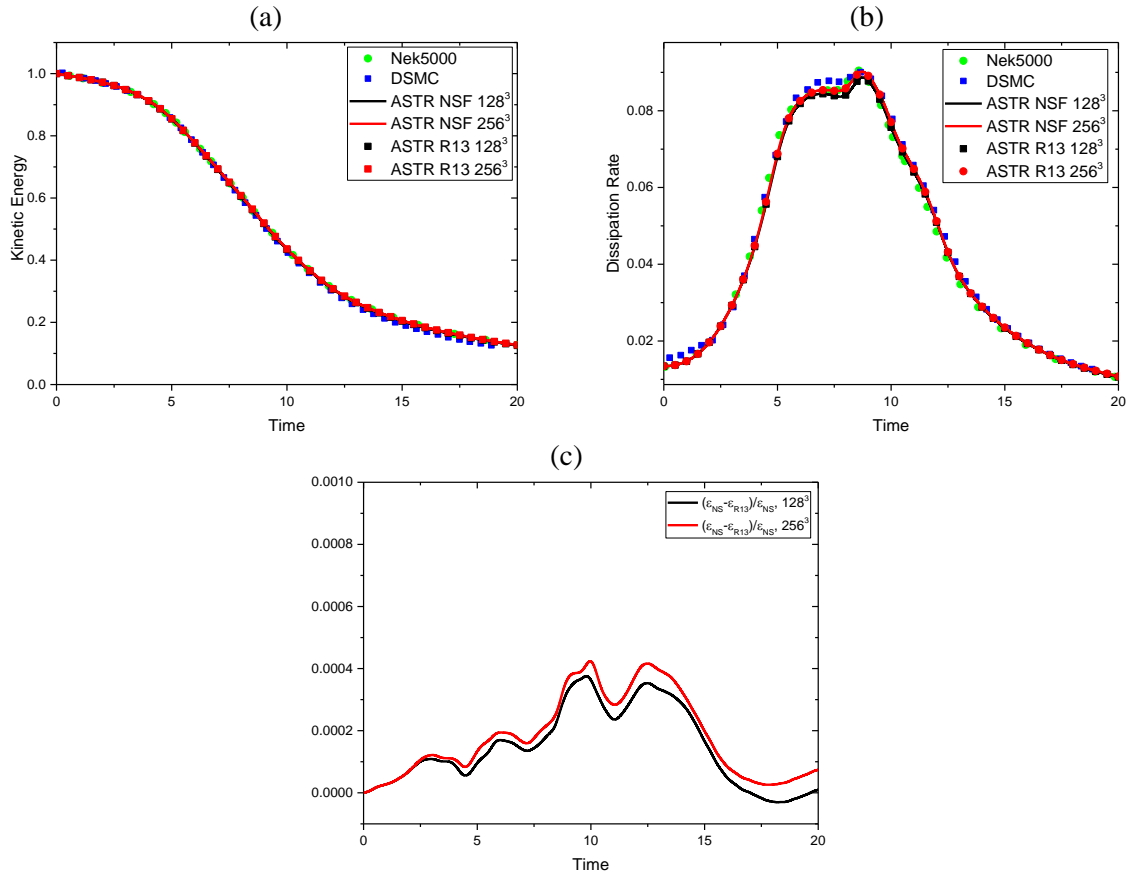


Figure 3 Evolution of kinetic energy (a), dissipation rate (b), and the difference in dissipation rate of TGV flow at $Kn=0.001$.

To highlight the importance of the moment equations, we further validate the development for TGV with a higher degree of rarefaction at $Re = 50$ and $Ma=2.5$ ($Kn=0.083$), in figure 4. The difference in the evolution of kinetic energy is still very small, meaning closure models have a negligible effect on the bulk effect of the shear tensor. However, the difference is obvious in the evolution of high-order statistics, e.g., the dissipation rate shown in figure 4 (b). The NSF predicted a higher level of dissipation rate than both the R13 and R26 models, especially around the peak of the dissipation rate. The results from the R13 and R26 models are close to each other, which means the usage of high-order closure for weak rarefied flow is not really necessary.

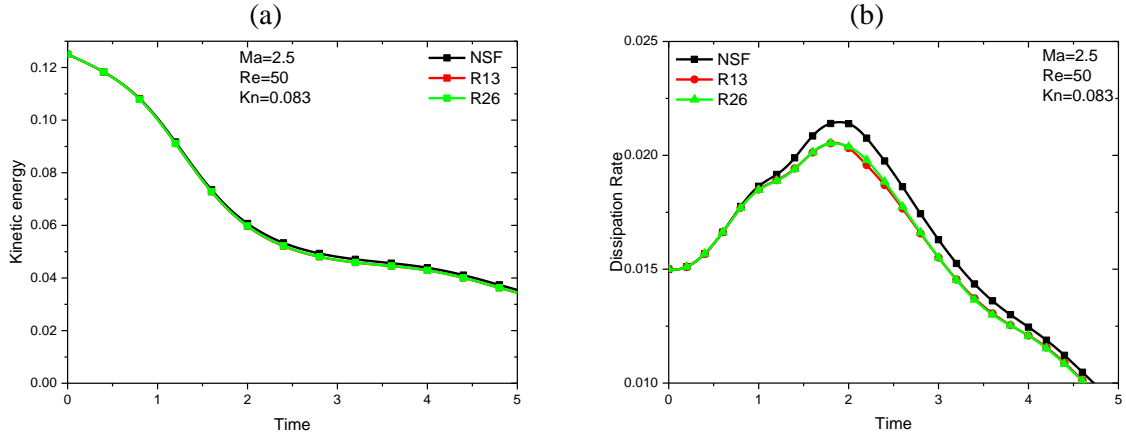


Figure 4 Evolution of kinetic energy (a), dissipation rate (b) of TGV flow at $Kn=0.083$.

4.2 Lid-driven cavity flow

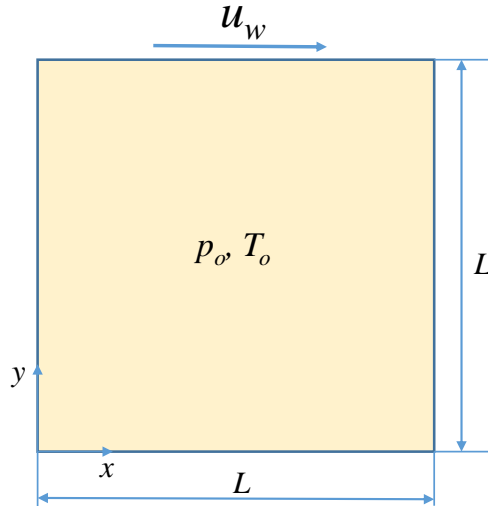


Figure 5 Configuration of driven cavity flow problem.

The validity of the implementation of the moment equations and their wall boundary conditions is examined on a 2D square lid-driven cavity flow, which is a standard benchmark problem to validate numerical accuracy. The length of the cavity edges is L and the lid moves at a velocity, u_w , as shown in figure 5. The origin of the coordinates sits at the left bottom corner of the cavity. The reference temperature and viscosity are $T_o = 273\text{K}$ and $\mu_o = 21.25 \times 10^{-6} \text{Pa} \cdot \text{s}$, respectively.

The rarefied gas flow of $Kn=0.1$ and 0.5 in a square-driven cavity with a length of L is calculated computed with the moment equations in comparison with the DSMC data (John et al 2010). The wall velocity is set to be 50 m/s so that Mach number is $Ma = 0.1625$. The relationship between Re , Kn , and Ma is readily obtained as

$$Ma = \sqrt{\frac{2}{\gamma\pi}} Re Kn. \quad (34)$$

The corresponding Reynolds number is $Re = 2.629$ and 0.5258 , respectively.

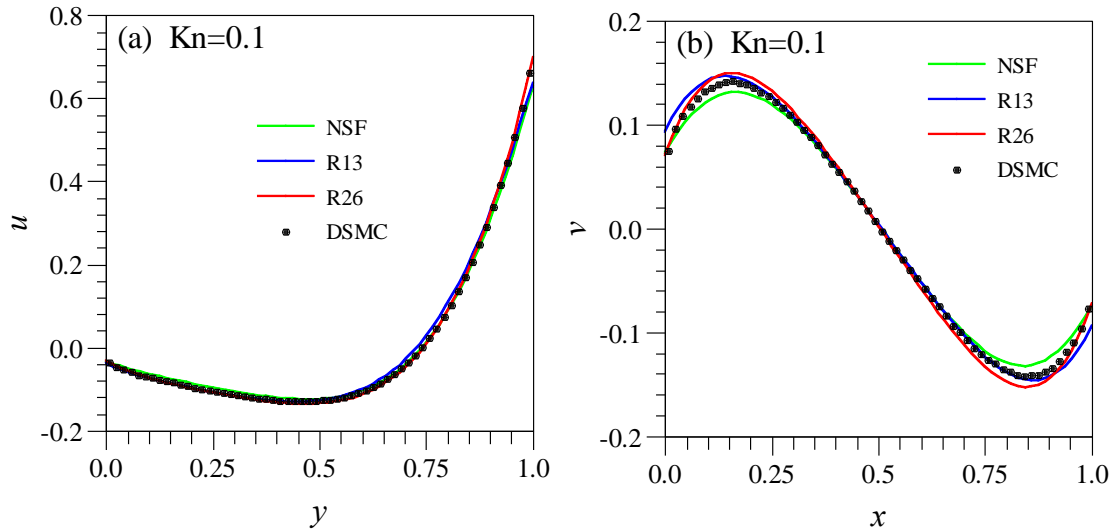


Figure 6 Velocity profiles along the lines through the cavity centre at $Kn = 0.1$.

Figure 3 shows the computed u and v -velocity components from the three macroscopic equation sets along the central vertical line and horizontal line, respectively, crossing the cavity centre at $Kn = 0.1$, in comparison with the DSMC data (John et al 2010). At the upper boundary of the slip regime of $Kn = 0.1$, the agreements between the macroscopic models and the DSMC data are good in general, apart from the slip velocity along the top moving lid wall. The NSF and R13 equations overpredict the slip velocity while the R26 equations agree with DSMC data well.

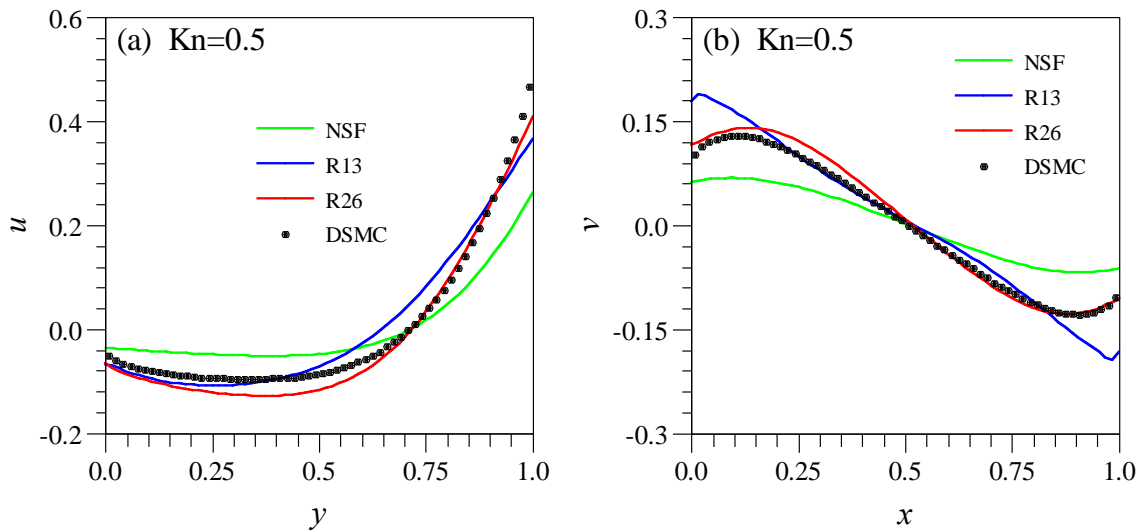


Figure 7 Velocity profiles along the lines through the cavity centre at $Kn = 0.5$.

For the case of $Kn = 0.5$ into the transition regime, the NSF equations overpredict the slip velocity on the top moving lid wall significantly in comparison with the DSMC data (John et al 2010), as indicated in figure 7(a). The v -velocity along the horizontal centre line from the NSF equations is significantly lower than the DSMC, as the result of the overpredicted slip velocity along the walls as shown in figure 7(b). On the other hand, the R26 moment equations follow the DSMC data reasonably well in both u and v in the x and y directions, respectively, apart from overpredicting the slip velocity slightly in comparison with the DSMC data. The results of the R13 equations are between the NSF and R26 equations, as expected.

5. Computational performance

As the number of the equations increases from the NSF equation set to the R26 moment equation set, the total CPU time increases accordingly. However, the parallel performance, such as the speedup, remains the same for the different levels of the equation sets.

6. Conclusions

The capability of the open-source CFD code, *ASTR*, has been extended to simulate non-equilibrium gas flow by adding several modules based on the Method of Moments. The Cartesian components of the higher rank moments are solved as primary variables. All of the added modules have been tested (i) Taylor Green Vortex (TGV); (ii) Lid-driven cavity flow. The validation cases have been compared to available data to ensure the accuracy of the implementation.

Acknowledge

This work is funded under the embedded CSE programme of the ARCHER2 UK National Supercomputing Service (<http://www.archer2.ac.uk>).

References

- CERCIGNANI, C. 1975 *Theory and Application of the Boltzmann Equation*. Scottish Academic Press, Edinburgh.
- CHAPMAN, S. & COWLING, T. G. 1970 *The Mathematical Theory of Non-uniform Gases*. Cambridge University Press.
- GAD-EL-HAK, M. 1999 The fluid mechanics of microdevices – The Freeman scholar lecture. *J. Fluids Eng.* **121**, 5-33.
- GALLIS, M.A., BITTER, N.P., KOEHLER, T.P., TORCZYNSKI, J.R., PLIMPTON, S.J., PAPADAKIS. 2017 Molecular-level simulations of turbulence and its decay. *Phys. Rev. Lett.* **118**, 64501.
- GRAD, H. 1949 On the kinetic theory of rarefied gases. *Commun. Pure Appl. Math.* **2**, 331-407.
- GU, X. J. & EMERSON, D. R. 2007 A computational strategy for the regularized 13 moment equations with enhanced wall-boundary conditions. *J. Comp. Phys.* **225**, 263-283.
- GU, X. J. & EMERSON, D. R. 2009 A high-order moment approach for capturing non-equilibrium phenomena in the transition regime. *J. Fluid Mech.* **636**, 177-216.
- GU, X. J., JOHN, B., TANG, G. H. & EMERSON, D. R. 2009 Heat and mass transfer of a rarefied gas in a driven micro-cavity. In: Proceedings of MNHMT09, MNHMT2009-18236.
- GU, X. J., EMERSON, D. R. & TANG, G. H. 2010 Analysis of the slip coefficient and defect velocity in the Knudsen layer of a rarefied gas using the linearized moment equations. *Phys. Rev. E* **81**, 016313, 2010.
- GU, X. J. & EMERSON, D. R. 2014 Linearized-moment analysis of the temperature jump and temperature defect in the Knudsen layer of a rarefied gas. *Phys. Rev. E* **89**, 063020.
- GU, X. J., BARBER, R.W., JOHN, B. & EMERSON, D. R. 2019 Non-equilibrium effects on flow past a circular cylinder in the slip and early transition regime. *J. Fluid Mech.* **860**, 654-681.
- John B., Gu, X. J. and D. R. Emerson, D. R. 2010 Investigation of heat and mass transfer in A lid-driven cavity under nonequilibrium flow conditions. *Numerical Heat Transfer, Part B*, **58**: 287–303.
- MAXWELL, J. C. 1879 On stresses in rarified gases arising from inequalities of temperature. *Phil. Trans. Roy. Soc. (Lond.)* **170**, 231-256.
- STRUCHTRUP, H. 2005 *Macroscopic Transport Equations for Rarefied Gas Flows*. Springer-Verlag, Berlin Heidelberg.

- STRUCHTRUP, H. & TORRILHON, M. 2003 Regularization of Grad's 13 moment equations: Derivation and linear analysis. *Phys. Fluids* **15**, 2668-2680.
- TAHERI, P. and STRUCHTRUP, H. 2009 Effects of rarefaction in microflows between coaxial cylinders. *Phys. Rev. E* **80**, 066317.
- TAHERI, P., TORRILHON, M. and STRUCHTRUP, H. 2009 Couette and Poiseuille microflows: Analytical solutions for regularized 13-moment equations. *Phys. Fluids* **21**, 017102.
- TAHERI, P. & STRUCHTRUP, H. 2010 An extended macroscopic transport model for rarefied gas flows in long capillaries with circular cross section. *Phys. Fluids* **22**, 112004.
- YOUNG, J. B., Calculation of Knudsen layers and jump conditions using the linearised G13 and R13 moment methods 2011 *Int. J. of Heat and Mass Transfer* **54**, 2902-2912.